npj | acoustics

Article

https://doi.org/10.1038/s44384-026-00045-w

Designing band gaps with randomly distributed sub-wavelength Helmholtz resonators

Check for updates

Paulo S. Piva[1], Art L. Gower[1] ✉ & I. David Abrahams[2]

It is well-known that band gaps for wave propagation, in the frequency domain, can be achieved by using periodically-arranged inclusions in a host material. However it has been challenging to design materials with broad band gaps or that have multiple overlapping band gaps. For periodic composites this difficulty arises because many different length scales would have to be repeated periodically within the same structure to have multiple overlapping band gaps. Here we present an alternative: to design band gaps with disordered materials. We show how to tailor band gaps by choosing any combination of Helmholtz resonators that are positioned randomly within a host acoustic medium. One key result is that, via analytical (asymptotic) analysis, we are able to derive simple formulae for the effective material properties, which work over a broad frequency range. These can therefore be used to rapidly design tailored metamaterials. We show that these formulae are robust by comparing them with high-fidelity Monte-Carlo simulations over randomly positioned resonant scatterers.

Metamaterials are artificially fabricated materials, usually of composite constructing, which have properties not found in nature; they are designed for specific and targeted applications[1]. Wave motion control is an important application for electromagnetics, elastodynamics, and acoustics. There are many examples of fabricated materials that can distort or bend the path that waves propagate along, allow negative refraction[2], block specific frequencies[3], or cloak (i.e. render invisible) certain parts of space[4–7]. In recent years, the focus on elastic and acoustic metamaterial theory and design has broadened to include non-reciprocal wave propagation[8], acoustic lenses[9], and optimal wave-absorbing layered media[10].

Among the various applications of acoustic metamaterials, the one most relevant to this work is the control of transmission through one or multiple layers, commonly realized via structures designed for absorption and reflection. A widely used strategy for enhancing sound absorption involves tuned resonant elements. Helmholtz resonators, in particular, are highly tunable[11] and, when combined in different configurations, can give rise to a variety of absorption and reflection phenomena in metamaterials, such as perfectly absorbing systems[12]. This flexibility allows to design compact materials with both broadband and targeted absorption spectrum[13,14].

In many applications, the design of metamaterials for wave control is often a heuristic process, which encourages heavy optimisation and machine learning techniques in the literature[15,16]. However, even after long and extensive computations to find an optimal metamaterial arrangement, small manufacturing changes/defects can lead to errors that significantly alter the band structure. For this reason, these materials require elaborate manufacturing techniques[17,18].

In this paper, we present a disordered (random) metamaterial, which can be designed to have broad as well as multiple localised (overlapping) low-frequency band gaps, that are robust to small changes in its micro-structure. We show how to design such metamaterials and, more importantly, derive simple explicit formulae for the band gaps which do not require heavy optimisation. One difficulty that has slowed progress in disordered materials is that the scattering response from any one configuration of resonators can be complicated; however we show here how to completely overcome this difficulty by combining ensemble averaging techniques[19–21] together with asymptotic homogenisation.

As an example, we develop our formulas for a mixture of split-ring resonators. A split-ring resonator, shown in Fig. 1a, is a type of Helmholtz resonator, characterised by a cavity-neck system with resonance peak located in the sub-wavelength range ($kb \leq 1$), shown in Fig. 1b. We choose this specific type of resonator because its scattered wave has been deduced from first principles[22].

To achieve multiple band gaps, we combine different types of sub-wavelength split-ring resonators, each with a different resonance frequency. By a band gap, we mean a frequency range where the average wave cannot propagate, but incoherent speckle may still propagate[23]. To the best of the authors' knowledge, there has been no clear consistent strategy to derive

[1]School of Mechanical, Aerospace and Civil Engineering, University of Sheffield, England, UK. [2]Department of Applied Mathematics and Theoretical Physics, University of Cambridge, England, UK. ✉e-mail: arturgower@gmail.com

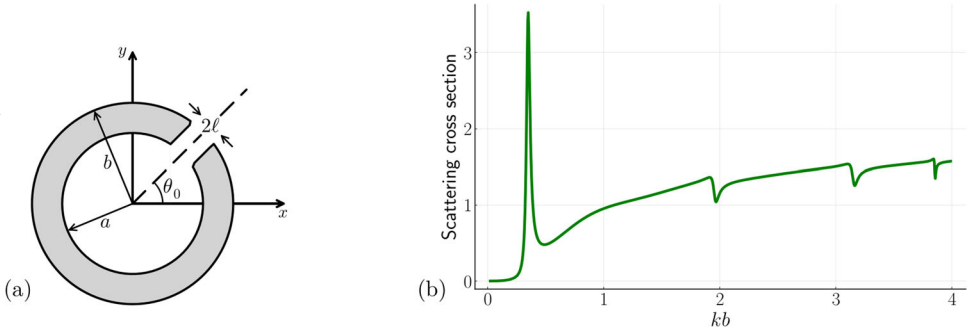


Fig. 1 | A split-ring resonator. The left figure (**a**) shows an illustration of a typical split-ring resonator. The right figure (**b**) shows the scattering cross section of a sound-hard 2D split-ring resonator with an aperture size of $2\ell = 0.1b$, and k is the wavenumber of the background medium.

simple formulae for effective-properties of a mix of different types of split-ring resonators. It has only been possible to derive effective-properties for a periodic array of identical sub-wavelength split-ring resonators[24–26]. To reach simple formulae, which are needed to easily design band gaps, asymptotic homogenisation is essential[24,27–30]. It is common to enforce that the resonators are sub-wavelength, as we also do in this work. However, care must be taken to accurately capture the resonance beyond the quasi-static limit.

Effective material properties, for example mass density and speed of sound, have been deduced for a circular cluster of 2D particles (rods)[31–34]. To summarise, these papers consider a given particle configuration and, in the long-wavelength limit, determine the effective-properties of a single equivalent circle that would reproduce the same scattering as the entire cluster. This can lead to effective-properties which depend on frequency[33,34] and on a specific particle configuration. Dependence on the particle configuration leads to extra degrees of freedom to tune the effective-properties, but also has drawbacks: it can be computationally difficult to calculate for a large number of particles, and then also requires fabricating material with exact particle positions. To remove the dependence on the particle configuration it has been suggested to average over the effective-properties[32,33]. However, this is not the same as averaging over the scattered wave from a disordered material, and can also have a high computation cost.

One concern raised in many papers[20,35,36] is that beyond the leading order low-frequency limit, there is no unique way to calculate effective-properties. That is, calculating the properties for an effective cylinder[31,32] can lead to different results than calculating the properties for an effective slab[20], despite both having the same set of scatterers or microstructure. However, to include resonance effects, it is necessary to include terms beyond the low-frequency approximation, so the question is how to do this correctly? Here we show how to deduce frequency-dependent effective-properties directly from the dispersion equation for the effective wavenumber, which is valid for any material shape and frequency[20]. From this solid ground, we then use asymptotic expansions that capture the resonance of the scatterers. As a result, our method leads to effective-properties which provide the correct average wave scattering from a disordered material.

To showcase how simple it is to use our formulae to design a material, and motivate the reader for the rest of the paper, we present an acoustic version of a device that splits a signal into two different channels, or waveguides, dependent on its frequency components shown in Fig. 2. These devices are known as frequency demultiplexers. They are used in digital computing and telecommunication networks, and are often designed via tailored periodic structures, as in[37], or through black-box optimisation, as in[38]. In contrast, as illustrated in Fig. 2, we are able to produce with little effort a low insertion loss ($\lesssim$5 dB) and high contrast ($\sim 10-20$ dB) demultiplexer using only randomly placed and oriented resonators, which has similar performance compared to the microchip in [Figure 4b [38]]. Figure 2 also shows the amplitude of the transmitted waves for two wavelengths of high contrast in transmission through the top and bottom waveguides. We note that we used only one configuration of randomly placed particles for all the results shown in Fig. 2.

Designing devices, such as the demultiplexer in Fig. 2, with randomly oriented resonators makes them robust to manufacturing defects in terms of the positioning of each resonator. This is because the formulae for the effective-properties are agnostic to the position and orientation of the resonators. Alternatively, the performance could be further enhanced by optimising the position of the resonators.

Results

In this section, we present our main results: the effective-properties of the metamaterial. Later, in section **Low-frequency expansion**, we show how to derive these results. The focus below is on how to use the effective-properties, followed by examples, and to present high-fidelity Monte-Carlo validation.

The resonators in the material can have varied sizes, geometry, and properties, although for ease of exposition we illustrate the case of circular sound-hard split-ring resonators in 2D, as shown in Fig. 3. Let us consider N different types of sound-hard Helmholtz resonators, which are randomly distributed in a homogeneous background medium (see Fig. 3). The properties of the resonators feed into the formulae for the effective bulk modulus ($\beta_\star$) and effective mass density ($\rho_\star$), which are given by:

$$\beta_\star(k) = \frac{\beta}{(1-\varphi) + \sum_{j=1}^{N} z(\lambda_j)\phi_j} \quad \text{and} \quad \rho_\star = \rho\frac{1+\varphi}{1-\varphi}, \tag{1}$$

where β and ρ are the bulk modulus and mass density of the background medium, ϕ_j is the volume fraction of the j-th type of resonator, with $\varphi = \sum_{j=1}^{N}\phi_j$ being the total volume fraction of the resonators (including their interiors). For two dimensions, the volume fraction reduces to the ratio of the area occupied by a phase to the total area of the material. We call $z(\lambda_j)$ the *resonance factor* of the j-th resonator type derived via careful matched asymptotic analysis[22,25]. The resonance factor depends only on the geometrical properties of the resonator and the wavenumber k of the background medium. When hitting a resonance $z(\lambda_j)$ increases in magnitude, and when there is no contribution from the resonator then $z(\lambda_j)$ is small. See section **Scattering by a single resonator**, for more details and see section **T-matrix of a single resonator** for a derivation of a formula for $z(\lambda_j)$ for split-ring resonators.

The effective bulk modulus $\beta_\star$ is frequency-dependent, and its behaviour depends on the geometry of each resonator in the mixture. $\beta_\star(k)$ is the most important parameter to design band gaps for metamaterials, since the effective mass density $\rho_\star$ does not depend on frequency and only increases when adding more resonators to the mixture.

Below we show three examples on designing band gaps by using a layer of randomly placed resonators, as illustrated in Fig. 3. For all the examples we assume that the background medium is air ($\rho = 1\text{kg/m}^3$, $\beta = 117.6\text{kPa}$). After the examples, we show how high-fidelity Monte-Carlo simulations closely agree with our simple formulae for a broad frequency range.

Example 1: changing volume fractions

Consider a material filled with a single species of thin-walled split-ring resonator ($a = b$ and one fixed value of the aperture 2ℓ in Fig. 1a). To help

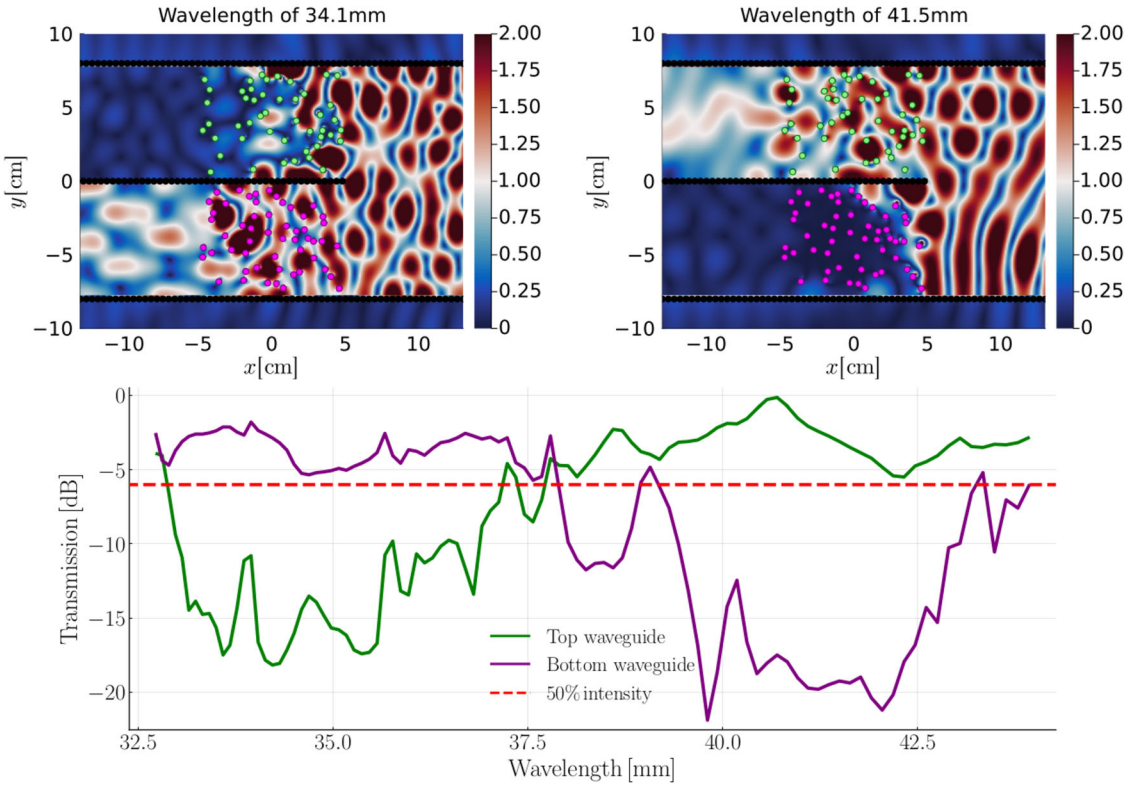


Fig. 2 | Frequency demultiplexer. The top two images show a very simple frequency demultiplexer we designed using randomly placed Helmholtz resonators to illustrate our results. In the top two images a harmonic plane source (of amplitude 1) travels from right to left inside a waveguide which then splits into two smaller waveguides at $x = 5$cm. The top waveguide filters out waves with wavelengths close to 34.1 mm due to the scattering by resonators represented by green circles, with an aperture of $2\ell =$ 0.2 mm. In contrast, the bottom waveguide filters out waves with wavelengths close to 41.5 mm with resonators represented by magenta circles, with an aperture of $2\ell =$ 0.04mm. All resonators have rigid thin walls ($a = b = 2$ mm in Fig. 1a), (uniformly) randomly placed and oriented in air. The colour bar shows the amplitude of the total wave (incident plus scattered). The graph shows the transmitted intensity into each waveguide, calculated in dB. The values of transmission are calculated as the average intensity of the wave on the left-hand side of the region containing particles in each of the waveguides. Wavelengths from 33 to 38 mm are mostly transmitted through the lower waveguide, while wavelengths from 38 to 43 mm are mostly transmitted through the upper waveguide.

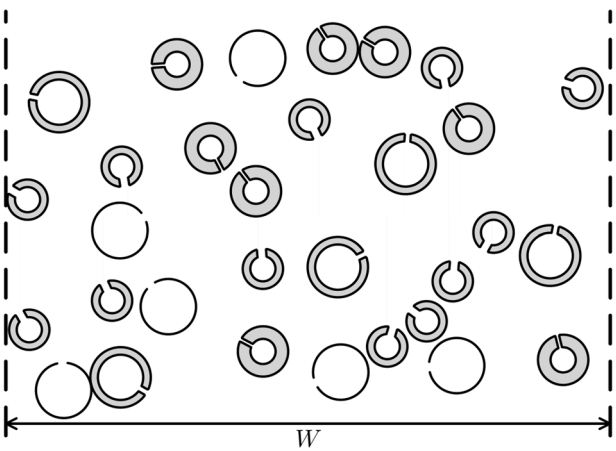


Fig. 3 | A layer of metamaterial. Representation of one possible configuration of split-ring resonators in a layer of width W.

illustrate the results, we consider a layer of width W (infinite length), shown in Fig. 3, and calculate its effective transmission coefficient by assuming the material is homogeneous with the properties given by (1).

From the results, shown in Fig. 4b, we see that only a small percent of resonators are needed to completely stop transmission through this layer. As the volume fraction increases, the minimum grows wider and shifts towards higher frequencies. With only $\varphi = 6\%$ volume fraction, we reach a band gap around 140Hz, which shows that a thin layer of the proposed metamaterial is a good candidate for a sound-insulating material. To broaden the band gap, it is possible to either increase the width of the metamaterial layer W, or the volume fraction of resonators φ (see Fig. 4b).

Another lesson to learn from Fig. 4a is that the minimum of the curve $\varphi = 1\%$ is very close to the resonance frequency of a single thin-walled resonator, shown in 1b. However, the minimum of the $\mathrm{Im}[\beta_\star]$ curves shifts to higher frequencies as φ increases because of multiple scattering effects between the resonators. Being able to predict this minimum, with our formulae (1), rather than finding it through trial and error, can save time and resources in most applications.

Finally, because Fig. 4a has non-dimensional independent variables, note that increasing the size of the resonators, while thickening the layer, would lead to the band gap shifting to a lower frequency range.

Example 2: broadening band-gaps

To achieve a broader band gap, or separate band gaps, we could use layers of random resonators of the type discussed in Example 1. Instead, we show a case with two types of thin-walled resonators to the formulae (1) with multiple types of resonators. The two types have different radii, $b_1 \neq b_2$, and aperture sizes, $\ell_1 \neq \ell_2$. The results are presented in Fig. 5.

In Fig. 5(a) we notice that when the aperture ℓ_2 decreases, the graph of $\mathrm{Im}[\beta_\star]$ transitions from having one minimum to two distinct minima. The appearance of the second dip is due to the resonance frequencies of the two types of resonators moving further apart as we decrease ℓ_2. The overall result in the transmission (Fig. 5b) is a wide band gap, which separates into two thinner band gaps as ℓ_2 decreases.

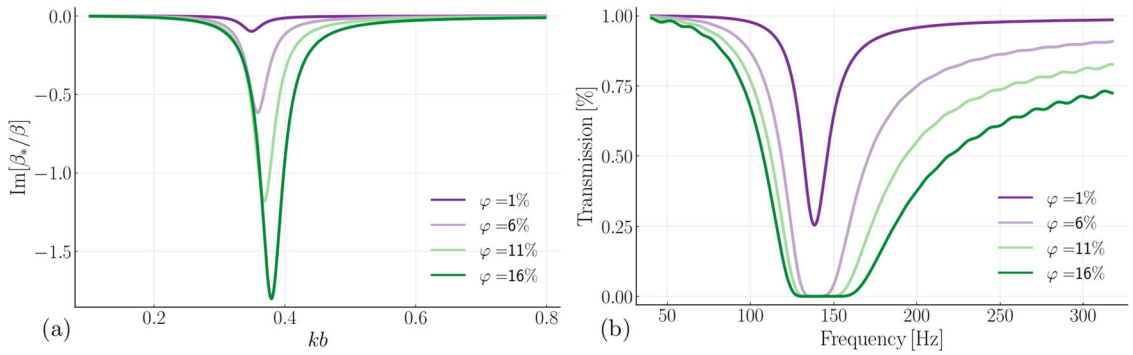


Fig. 4 | Band gap from a single type of resonators. a shows the imaginary part of the effective bulk modulus $\beta_\star$ and (**b**) the magnitude of the transmission coefficient through a layer of width $W = 32$ mm. The layer is composed of thin-walled randomly-positioned Helmholtz resonators with radius $b = 0.4$ mm, and k is the background wavenumber. The aperture size of the resonators is $\ell = 0.05b$. Each curve has a different volume fraction of resonators.

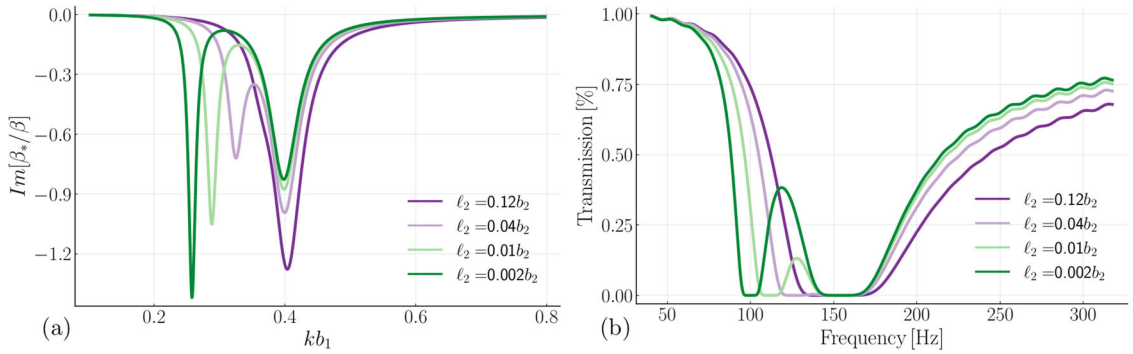


Fig. 5 | Band gap broadening with two types of resonators. a shows the imaginary part of the effective bulk modulus and (**b**) shows the magnitude of the transmission coefficient through a layer of width $W = 32$ mm. The layer is composed of thin-walled random Helmholtz resonators with radius $b_1 = 0.4$ mm and $b_2 = 0.2$ mm. The total volume fraction of resonators is $\varphi = 15\%$, and half of them ($\phi_1 = 7.5\%$) have an aperture size of $\ell_1 = 0.1b_1$. Only the aperture size ℓ_2 of the other half of the resonators changes between curves.

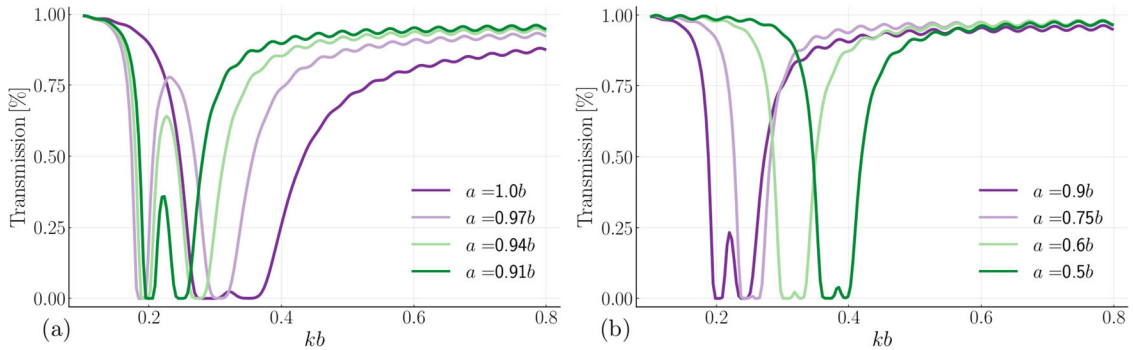


Fig. 6 | Band gap with three types of resonators. Both graphs, (**a**) on the left and (**b**) on the right, show the transmission coefficient through a metamaterial of width W = 32 mm filled with randomly positioned resonators, all with the same outer radius b.The total volume fraction of resonators is $\varphi = 12\%$, with a third of them having an aperture size of $\ell_1 = 0.05b$, another third with $\ell_2 = 0.01b$, and the final third with $\ell_3 = 0.005b$. For each curve we use a different inner radius a for all the resonators.

Example 3: shifting band-gaps

Here we consider a mix of three types of resonators, each with a volume fraction of $\phi_j = 4\%$ for $j = 1, 2, 3$. We use three types just to showcase that we can. Each resonator has a different aperture size, but the three types have the same outer and inner radius b and a, for simplicity. Our goal is to show how the band-gaps shift when the wall of the resonators becomes thicker. Increasing the thickness causes a non-intuitive change in the resonance which can only be predicted with our effective-properties (1).

The transmission results for different values of the inner radii a, which changes the wall thickness, are shown in Fig. 6 below. In Fig. 6a we see that as a gets smaller, and the wall thickness increases, the resonant frequency gets lower, however there is a limit to this effect. In Fig. 6b we see that a further decrease in a makes the resonant frequency become higher again, as well as lessening the strength of the resonance. These effects illustrate the need for our formulae to guide the design process.

Monte-Carlo validation

When dealing with disordered materials it is often impractical to predict the precise wave response of the material for each possible configuration of the microstructure. To reach our effective formulae (1) we used ensemble averaging techniques [39], which lead to practical and explicit results. In this

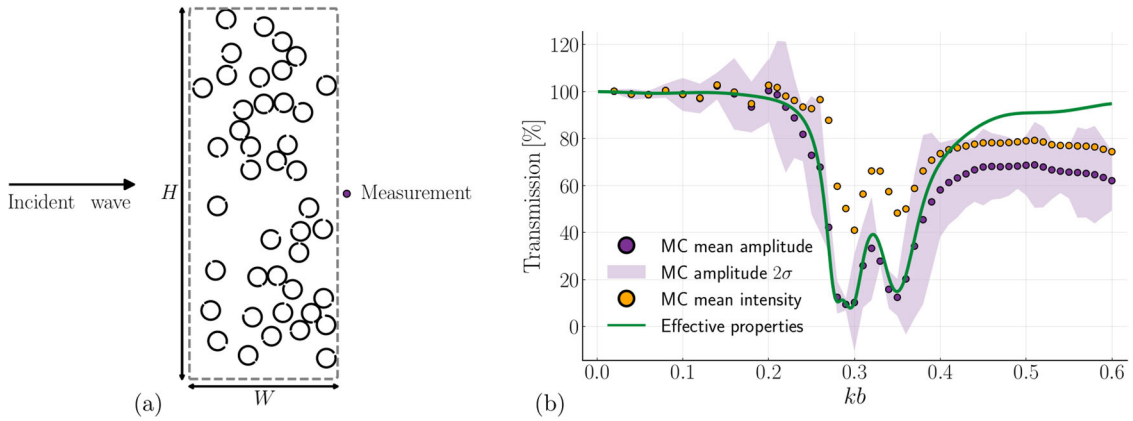


Fig. 7 | Monte-Carlo simulations for a layer. a shows one realisation used for our Monte-Carlo (MC) simulations, where resonators are placed within a layer of width $W = 20b$, height $H = 200b$, and b is the resonator radius. An incident plane wave comes from the left and the total field is then measured at a point at half height and one radius away from the layer. This simulation is repeated many times, each with a different configuration of resonators, and then the average MC field is compared with a transmission coefficient calculated by using the effective-properties (1), shown on the right (**b**). For the MC we use three types of thin-walled resonators, each with 4% volume fraction, but with different aperture sizes $\ell_1 = 0.05b$, $\ell_2 = 0.01b$, and $\ell_3 = 0.005b$. In total 5000 different configurations are calculated for the MC results in (b), and σ is the 2 × the standard deviation.

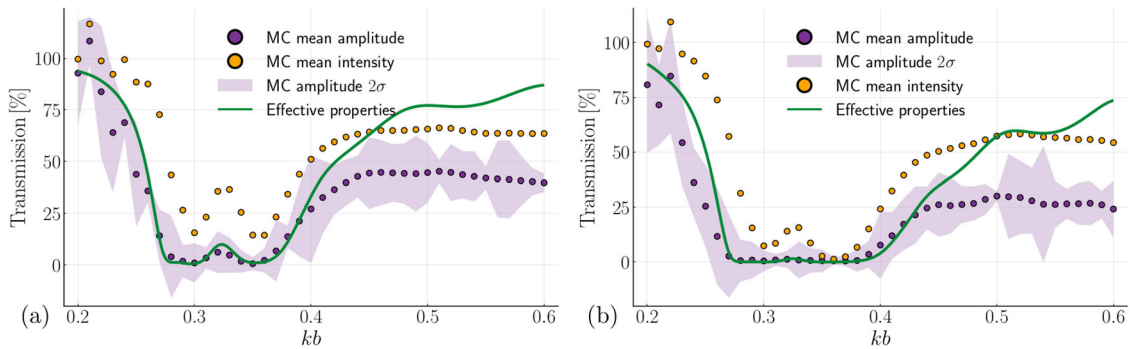


Fig. 8 | Zero transmission with Monte-Carlo simulations. Results of 5000 different configurations of Monte-Carlo (MC) simulations for the same setup as in Fig. 7, however with double (**a**), and triple (**b**), the volume fraction of each type of resonator in the mixture. In total, we have $\varphi = 24\%$ (**a**), and $\varphi = 36\%$ (**b**), volume fraction of resonators in the layer.

section we validate these formulae by using high-fidelity Monte-Carlo simulations for both a layer and circle filled with resonators. We also highlight some advantages and disadvantages of disordered metamaterials in general.

To get an exact match with a high-fidelity simulation, we need to perform simulations of wave scattering from one configuration at a time, where the resonators do not overlap and their positions are randomly chosen, see[40] and references within for details on how to achieve this. Some noteworthy references include[41,42]. The average wave is then calculated by taking the average total wave over all simulations. This is what we mean by a high-fidelity Monte-Carlo simulation. The mathematical details on ensemble averaging and the Monte-Carlo method are given in section **Ensemble average and multiple scattering**; here we focus mostly on showing the results.

We begin with the case of a layer filled with resonators and an incident plane wave. This is a case which is simpler to understand, though Monte-Carlo simulations can be challenging as the layer needs to be very tall, large H in Fig. 7, as the effective theory assumes the layer is infinitely extent.

We perform a high-fidelity Monte-Carlo simulation for a plane incident wave, with wavenumber k, scattered by randomly distributed and randomly oriented thin-walled split-ring resonators ($b = a$ in Fig. 1a) inside a long strip shown in Fig. 7a. The transmitted field is measured one radius away from right-hand side of the layer as also illustrated in Fig. 7a. This simulation is repeated many times, and the average transmission $\langle u \rangle$ is compared with the average intensity $\langle |u|^2 \rangle$, and the prediction from the effective-properties formulae (1) in Fig. 7b below. The runtime of the MC simulation was over 24 hours, with parallelization, and using all computational power available, while the effective formulas are computed in less than a second, using only a fraction of the computational power.

In Fig. 7b we see that the average transmission calculated using the effective-properties (1) accurately matches the average from Monte-Carlo (MC) $\langle u \rangle$ in the frequency range $kb \lesssim 0.4$ which includes the resonant frequencies, and agrees with our derivations in section **Low-frequency expansion**. The MC mean intensity $\langle |u|^2 \rangle$ is higher than the MC mean amplitude, specially around resonance, due to phase cancellation when calculating $\langle u \rangle$; see discussion below (18) in section **Ensemble average and multiple scattering** for more details. To qualitatively show the difference between mean amplitude and mean intensity, and better highlight the band gap as discussed in section **Introduction**, we provide two examples with the same setup as Fig. 7, except with two and three times more resonators respectively in the layer, shown in Fig. 8 below.

In Fig. 8, even when the average wave is completely blocked by the layer (zero transmission), the average intensity is not zero as it is in a speckled or incoherent form[23]. This incoherent part is lost when taking the average of the field, due to phase cancellation, but not in the average intensity. This type of band gap, introduced in section **Introduction**, is more general than the usual definition of a band gap for periodic materials, as some part of the wave does get transmitted.

An important feature from Figs. 7b and 8 is that each realisation of the Monte-Carlo simulation is close to the MC mean amplitude for $kb \lessapprox 0.4$, especially in the band gap region. That is, the purple shaded area has a 95%

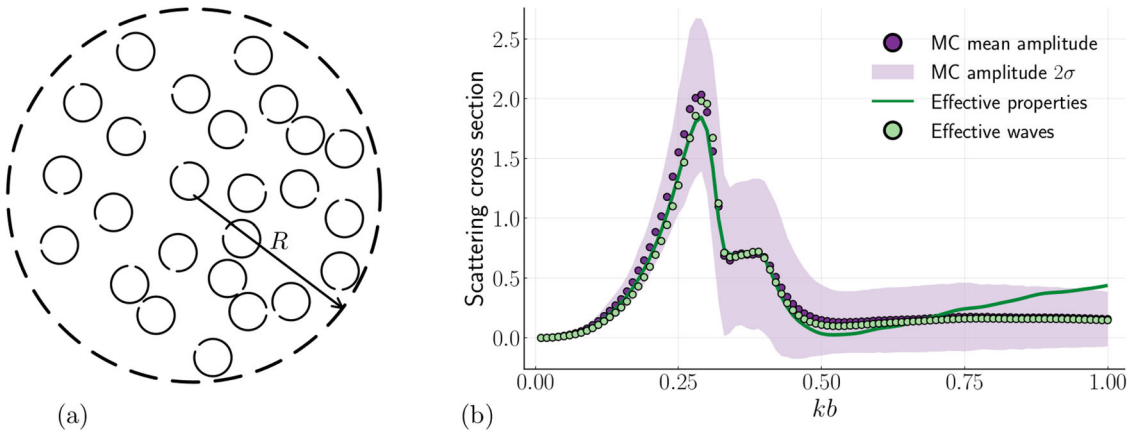


Fig. 9 | Monte-Carlo simulations for a circle. a shows one configuration of resonators used for our Monte-Carlo (MC) simulations. The resonators are placed randomly within a circle of radius $R = 20b$. An incident plane wave comes from the left and the resulting scattering cross section is shown in (**b**) on the right for three different methods: MC simulations, the effective waves method[20], and by using the effective-properties formulae (1). The aperture size of all resonators is $\ell = 0.05b$, the volume fraction is $\varphi = 10\%$ in all 40,000 configurations of the MC simulations, and σ is the standard deviation. The scattering cross section (2) was calculated with the first nine scattering coefficients $\langle \mathcal{F}_n \rangle$ in (2).

statistical confidence (2σ). This suggests a powerful design strategy: 1) first use the effective formulae to decide on what types of resonators to use, given some target band diagram, then 2) produce one realisation with the resonators randomly placed, and finally 3) perform a local optimisation to adjust the position of the resonators to further refine the transmission or reflecting properties. This design strategy would be much less computationally intensive than pure optimisation strategies used in the literature[15,16,38], as we discussed in section **Introduction**.

It is important to note that some MC points between $kb = 0.1$ and $kb = 0.22$ in Figs. 7b and 8 exceed 100%. If the height of the simulation doman H was infinite, and enough Monte-Carlo simulations (MC) were performed, then the average intensity must not exceed 100%. In our case, the transmission above 100% is due to the finite height H: the top and the bottom of the finite simulation domain leads to a diffracted wave which for specific frequencies tips the transmission over 100%. This has only a noticeable effect for one frequency in our results.

Our effective formulae (1) are valid for materials of any shape or size[20,43]. In particular, a circle filled with resonators leads to finite size Monte-Carlo simulations (MC)[43,44] which makes validation far simpler. See Fig. 9a for an illustration.

Our goal here is to compare three different methods to calculate the scattering cross section of a circle filled with resonators: 1) MC simulations, 2) a circle with the effective-properties (1), and 3) the effective waves methods[20,43] which works beyond low frequencies. The results are shown in Fig. 9b. The runtime of the MC simulation was over 5 hours, with parallelization, and using all computational power available. The effective waves method and effective formulas are computed in over 40 min and a few seconds respectively, using only a fraction of the computational power.

When performing MC for a circle filled with resonators, we make use of the rotational symmetry to greatly reduce the computational cost of calculating the scattering cross section, see[44] for details. For the circle with either effective-properties, or using the effective waves methods[20,43], the scattering cross section becomes:

$$\langle \Sigma_{sc} \rangle = \frac{2}{kR} \sum_{n=-\infty}^{\infty} |\langle \mathcal{F}_n \rangle|^2, \tag{2}$$

where R is the radius of the metamaterial, and $\langle \mathcal{F}_n \rangle$ are the average material coefficients defined in section **Ensemble average and multiple scattering**.

The results in Fig. 9b again show that the mean of MC data is close to the results using the simple formulae for the effective-properties at lower frequencies $kb \lesssim 0.7$. The effective-properties are deduced as a low-frequency asymptotic approximation of the effective waves method, and it can be seen in Fig. 9 that these two methods match for lower frequencies.

Figure 9 also shows that the effective waves method matches the Monte-Carlo results for all frequencies. This would not be expected for all resonators and volume fractions, because the effective waves method may lose accuracy when strong scattering is present. This is because strong scattering can trigger multiple effective wavenumbers[45], and the effective wave method shown here only considers one effective wavenumber. Despite being more accurate, the effective waves method has a significant drawback: it requires a much more elaborate calculation[43] than the formulae (1), which makes it less useful than the effective formulae for designing metamaterials.

Discussion

We have introduced a disordered composite metamaterial, consisting of sub-wavelength Helmholtz resonators. Having small resonators compared to the wavelength ($kb < 1$) allowed us to deduce, from first principles, formulae for both effective bulk modulus and effective mass density (1). These formulae were validated against high-fidelity Monte-Carlo simulations for both a layer and a circle filled with resonators. Using our effective formulae, we are able to quickly design broad frequency band gaps without using multiple layers, periodicity, or heavy optimisation methods. In future work, we plan to expand our results to higher order in kb and hence produce formulae that hold at higher frequencies. This would allow us to consider the effects of particle positioning, through the pair-correlation, and allow us to quantify the difference between, say, random, periodic and hyperuniform materials. At higher frequencies, or for thick-walled resonators, the effects of viscous dissipation are likely to become important, and so can be incorporated into the resonator apertures in the manner discussed in [22], or by more sophisticated asymptotic analysis.

Contrary to the standard approach with periodic media, the formulae we deduce are based on ensemble averaging over the possible positions and orientations of the resonators, which introduces both advantages and disadvantages. The key advantages are that: 1) we were able to easily deduce effective-properties for any mix of different types of resonators, and 2) the effective-properties are robust with respect to changes in position and orientation of the resonators, as shown by the motivation example in Fig. 2. However, the effective-properties in (1) do not give exactly the same results as any one specific configuration, and they also do not capture the average intensity of the scattered waves.

Despite using ensemble averaging in deriving (1), there are many applications for a single configuration of resonators. For example, the frequency demultiplexer in Fig. 2 with only one configuration of resonators

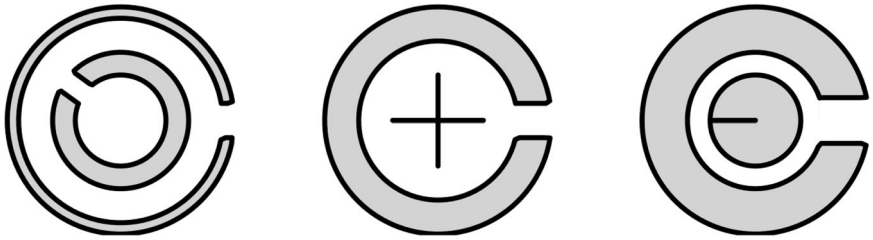


Fig. 10 | Alternative internal structures for Helmholtz resonators. Three examples of Helmholtz resonators with different resonance factors $z(\lambda)$.

generated randomly had a similar performance compared with the one achieved via heavy optimisation in [38]. In part this is due to the response of a single configuration being close to the mean response for low frequencies, as illustrated by the purple shaded region in Figs. 7, 8, 9 which represents two standard deviations of the mean.

Throughout the whole paper we only showed examples of split-ring resonators from[22,25,26]. However, the formulae for the T-matrix (6) has the same form for any sub-wavelength circular Helmholtz resonator (which has one aperture), like the ones depicted in Fig. 10, and the derived effective-properties (1) would have the same formula, although the resonance factor $z(\lambda)$ would change. Resonators with different internal structures should result in richer effective-properties for the metamaterial, as illustrated in Fig. 6 for thick walled split-ring resonators.

One interesting direction to explore as future work is to implement the enhanced design strategy described in section **Monte-Carlo validation**. This strategy consists of finding one specific configuration for the particles via optimisation while being guided by the overall band structure from the effective-properties (1). Another future avenue would be to investigate possible generalisations of the metamaterial presented. The simplest example is the three-dimensional case, where the Helmholtz resonators are spherical shells with a small aperture. Different from the case of long cylinders, small spheres could be used to produce compact versions of the metamaterial presented in three dimensions. Other than just acoustics, the case of sub-wavelength resonating structures in electromagnetism or elasticity could lead to interesting applications. For example, one could study how to embed sub-wavelength resonators in the building blocks of low-frequency operating machinery or other structures, to prevent harmful vibrations from propagating.

Methods

Here we derive the effective-properties (1) in three steps: scattering by a single resonator in section **Scattering by a single resonator**, scattering of the whole metamaterial in section **Ensemble average and multiple scattering**, and then an asymptotic low-frequency expansion in section **Low-frequency expansion**.

Scattering by a single resonator

Before calculating the acoustic response of the whole metamaterial, we need to describe how each resonator scatters waves. This is best done with the T-matrix method[46–48], which we describe below, as it facilitates calculations for multiple scattering.

Let the centre of the resonator be the origin of $\mathbb{R}^2$. We assume the incident wave is a regular function, which allows us to expand the incident wave in terms of a series of regular radial waves:

$$u_{\text{inc}}(\boldsymbol{r}) = \sum_{n=-\infty}^{\infty} g_n \mathrm{V}_n(k\boldsymbol{r}) \quad \text{with} \quad \mathrm{V}_n(k\boldsymbol{r}) = \mathrm{J}_n(kr)\,\mathrm{e}^{\mathrm{i}n\theta}, \tag{3}$$

where $\boldsymbol{r} \in \mathbb{R}^2$, k is the wavenumber, J_n is the Bessel function of the first kind, and (r, θ) are polar coordinates of $\mathbb{R}^2$. Note that the time-harmonic dependence $\mathrm{e}^{-\mathrm{i}\omega t}$ is assumed throughout the paper for both incident and scattered waves, where ω is the angular frequency, and $k = \omega/c$, where c is the speed of sound in the background medium.

Due to the linearity of the Helmholtz equation, the total field is given by the superposition of the incident wave and the scattered field from our resonator:

$$u_{\text{tot}}(\boldsymbol{r}) = u_{\text{inc}}(\boldsymbol{r}) + u_{\text{sc}}(\boldsymbol{r}),$$

and, outside the resonator, the scattered field can be represented as a series of outgoing radial modes:

$$u_{\text{sc}}(\boldsymbol{r}) = \sum_{n=-\infty}^{\infty} f_n \mathrm{U}_n(k\boldsymbol{r}), \text{ for } r = |\boldsymbol{r}| > b, \tag{4}$$

where b is the outer radius of the resonator, f_n are the scattering coefficients, and the outgoing radial modes are given by:

$$\mathrm{U}_n(k\boldsymbol{r}) = \mathrm{H}_n(kr)\,\mathrm{e}^{\mathrm{i}n\theta},$$

with H_n being the Hankel function of the first kind. The usual superscript (1) on the Hankel function is suppressed here and henceforth for clarity.

To determine the scattered field, we need to apply boundary conditions at the walls of the resonator. The result of solving the boundary conditions can be expressed in terms of the T-matrix which relates the incident wave to the scattered waves through:

$$f_n = \sum_{m=-\infty}^{\infty} T_{nm} g_m, \tag{5}$$

where T_{nm} are the elements of the T-matrix. We deduce the T-matrix for a circular Helmholtz resonator with sound-hard walls (Neumann boundary conditions) and outer radius b in section **T-matrix of a single resonator**, which reads:

$$T_{np} = -\frac{\mathrm{J}'_{\mathrm{p(kb)}}}{\mathrm{H}'_{\mathrm{p(kb)}}}\delta_{np} - \frac{\mathrm{i}\mathrm{e}^{-\mathrm{i}(n-p)\theta_0}}{\pi \mathrm{H}'_n(kb)\mathrm{H}'_p(kb)} z(\lambda), \tag{6}$$

where θ_0 is the orientation of the aperture (anticlockwise angle with the x-axis), prime denotes differentiation with respect to the argument, and λ is a set of properties that identifies one type of resonator.

In section **Low-frequency behaviour of the resonance factor**, we use a closed form for $z(\lambda)$ for the split-ring resonator in Fig. 1, which is fully characterised by $\lambda = \{kb, ka, k\ell\}$ with outer radius b, inner radius a, and aperture of ℓ. However, the formula (6) is the same for any circular resonant structure, with only $z(\lambda)$ changing, with some examples illustrated in Fig. 10.

To determine the resonance factor $z(\lambda)$ for a different resonator, one should redo the asymptotic calculations in[22] for its specific internal geometry, and then repeat the deduction in section **T-matrix of a single resonator** to arrive at (6). Similarly, we could easily adapt (6) to incorporate the case of multiple apertures in the same resonator.

T-matrix of a single resonator

In this section, we deduce the T-matrix for a split-ring Helmholtz in (6) and use an expression for $z(\lambda)$ in (27) combined with (28) for a split ring resonator.

Consider a resonator with outer radius b, inner radius a, aperture size 2ℓ, and orientation θ_0, as shown in Figure 1. Let us obtain the scattered field for the incident plane incident wave:

$$v_{\rm inc}(\boldsymbol{r}) = \mathrm{e}^{\mathrm{i}kr\cos(\theta-\theta_{\rm inc})},$$

Using [Equation (3.1) [22]] we can calculate the scattered field for $\theta_0 = 0$ which in our notation becomes

$$v_{\rm sc}(\boldsymbol{r}) = \mathrm{A}\mathrm{U}_0(k\widetilde{\boldsymbol{r}}) + \sum_{n=-\infty}^{\infty} c_n \mathrm{U}_n(k\boldsymbol{r}), \tag{7}$$

where $\widetilde{\boldsymbol{r}} = \boldsymbol{r} - b(\cos(\theta_0), \sin(\theta_0))$ is the aperture location, c_n and A are coefficients given by [Eqs. (3.4) and (3.6) respectively [22]]. To obtain the scattered field for $\theta_0 \neq 0$, we rotate the coordinate system $\theta \to \theta - \theta_0$, followed by the rotation of the incident wave $\theta_{\rm inc} \to \theta_{\rm inc} - \theta_0$. These rotations leave the incident wave unaltered while rotating the resonator by an angle of θ_0 which together with [Equation (3.1) [22]] results in:

$$\begin{aligned} A &= -z(\lambda)\sum_{p=-\infty}^{\infty} \frac{\mathrm{i}^p kb}{\mathrm{H}'_p(kb)} \mathrm{e}^{\mathrm{i}p(\theta_0-\theta_{\rm inc})}, \\ c_n &= -\mathrm{i}^n \frac{\mathrm{J}'_n(kb)}{\mathrm{H}'_n(kb)} \mathrm{e}^{-\mathrm{i}n\theta_{\rm inc}} - \frac{A}{2}\frac{\mathrm{Q}_n(kb)}{\mathrm{H}'_n(kb)} \mathrm{e}^{-\mathrm{i}n\theta_0}, \end{aligned} \tag{8}$$

where $\mathrm{Q}_n(x) = \mathrm{J}_n(x)\mathrm{H}'_n(x) + \mathrm{J}'_n(x)\mathrm{H}_n(x)$, and the prime notation denotes the derivative with respect to the argument. We call the function $z(\lambda)$ the resonance factor and it is defined by (27) in section **Low-frequency behaviour of the resonance factor**.

To rewrite (7) in terms of a T-matrix, shown in (5), we need to express all the terms centred at the origin, which leads us to use Graf's addition theorem to rewrite the monopole term evaluated at $k\widetilde{\boldsymbol{r}}$ in the form:

$$\mathrm{U}_0(k\widetilde{\boldsymbol{r}}) = \sum_{n=-\infty}^{\infty} \mathrm{J}_{-n}(kb)\mathrm{e}^{\mathrm{i}n(\pi-\theta_0)}\mathrm{U}_n(k\boldsymbol{r}),$$

which substituted into (7) leads to

$$v_{\rm sc}(\boldsymbol{r}) = \sum_{n=-\infty}^{\infty} d_n \mathrm{U}_n(k\boldsymbol{r}), \text{ with } d_n = c_n + \mathrm{A}\mathrm{J}_n(kb)\mathrm{e}^{-\mathrm{i}n\theta_0}. \tag{9}$$

Next, the T-matrix (5) relates any incident wave to the scattered wave, so we need to rewrite any incident wave $u_{\rm inc}(\boldsymbol{r})$ in terms of plane waves to use the results above. To achieve this, we use the Jacobi-Anger expansion of the plane wave:

$$v_{\rm inc}(\boldsymbol{r}) = \mathrm{e}^{\mathrm{i}kr\cos(\theta-\theta_{\rm inc})} = \sum_{n=-\infty}^{\infty} \mathrm{i}^n \mathrm{J}_n(kr)\mathrm{e}^{\mathrm{i}n(\theta-\theta_{\rm inc})},$$

followed by a superposition of plane waves:

$$\begin{aligned} u_{\rm inc}(\boldsymbol{r}) &= \int_0^{2\pi} v_{\rm inc}(\boldsymbol{r})\mathrm{g}(\theta_{\rm inc})\mathrm{d}\theta_{\rm inc} = \int_0^{2\pi} \sum_n \mathrm{g}(\theta_{\rm inc})\mathrm{i}^n \mathrm{J}_n(kr)\mathrm{e}^{\mathrm{i}n(\theta-\theta_{\rm inc})}\mathrm{d}\theta_{\rm inc} \\ &= \sum_n [\mathrm{i}^n \int_0^{2\pi} \mathrm{g}(\theta_{\rm inc})\mathrm{e}^{-\mathrm{i}n\theta_{\rm inc}}\mathrm{d}\theta_{\rm inc}]\mathrm{V}_n(k\boldsymbol{r}). \end{aligned} \tag{10}$$

Without loss of generality, we choose the amplitude of the packet of plane waves $\mathrm{g}(\theta_{\rm inc})$ in (10) such that:

$$\mathrm{i}^n \int_0^{2\pi} \mathrm{g}(\theta_{\rm inc})\mathrm{e}^{-\mathrm{i}n\theta_{\rm inc}}\mathrm{d}\theta_{\rm inc} = g_n,$$

which implies that (10) now matches the form of any regular incident wave (3).

Now we need to perform the same operations on the scattered field $v_{\rm sc}$(9) from a plane wave to obtain the total scattered field from any incident wave $u_{\rm sc}$, which is possible due to the linearity of the Helmholtz equation and results in:

$$\begin{aligned} u_{\rm sc}(\boldsymbol{r}) &= \int_0^{2\pi} v_{\rm sc}(\boldsymbol{r})\mathrm{g}(\theta_{\rm inc})\mathrm{d}\theta_{\rm inc} = \sum_n \left[\int_0^{2\pi} d_n \mathrm{g}(\theta_{\rm inc})\mathrm{d}\theta_{\rm inc}\right]\mathrm{U}_n(k\boldsymbol{r}), \\ &= \sum_{n,p}\left[-\delta_{np}\frac{\mathrm{J}'_p(kb)}{\mathrm{H}'_p(kb)} + \frac{2\mathrm{e}^{-\mathrm{i}(n-p)\theta_0}}{(\pi kb)^2 h(\lambda)\mathrm{H}'_n(kb)\mathrm{H}'_p(kb)}\right] g_p \mathrm{U}_n(k\boldsymbol{r}), \end{aligned} \tag{11}$$

where we have used the Wronskian of Bessel-Hankel functions in the second line:

$$\mathrm{J}_n(x)\mathrm{H}'_n(x) - \mathrm{J}'_n(x)\mathrm{H}_n(x) = \frac{2\mathrm{i}}{\pi x}.$$

Finally by comparing (5), (6) and (11) we conclude that:

$$T_{np} = -\frac{\mathrm{J}'_{\mathrm{p(kb)}}}{\mathrm{H}'_{\mathrm{p(kb)}}}\delta_{np} + \frac{\mathrm{i}\mathrm{e}^{\mathrm{i}(n-p)\theta_0}}{\pi \mathrm{H}'_n(kb)\mathrm{H}'_p(kb)} z(\lambda), \tag{12}$$

which is the general T-matrix for a Helmholtz resonator using formulae in[22].

In section **Low-frequency expansion**, the T-matrix (6) is used to calculate the dispersion equation. However, as discussed in[20,44], only the average T-matrix over all orientations of the aperture θ_0 contributes to the dispersion equation. We call this orientation averaged version of (6) the isotropic T-matrix, which is given by terms in the diagonal terms of (6), as follows:

$$\overline{T}_n(\lambda) = -\frac{\mathrm{J}'_{\mathrm{n(kb)}}}{\mathrm{H}'_{\mathrm{n(kb)}}} - \frac{\mathrm{i}z(\lambda)}{\pi[\mathrm{H}'_n(kb)]^2}. \tag{13}$$

Ensemble average and multiple scattering

To account for different types of resonators in the metamaterial we need to first calculate the exact multiple scattering between the resonators, after which we will perform ensemble averaging as shown in[20,44,48]. We also borrow the notation from these references.

Let us number each resonator in the material. We denote the centre of the j-th resonator by $\boldsymbol{r}_j$, and the set of its properties by λ_j. As an example, if the j-th resonator is a split-ring resonator, shown in Fig. 1, we have the following set of properties:

$$\lambda_j = \{kb_j, ka_j, k\ell_j\}$$

where b_j is the outer radius, a_j the inner radius, and ℓ_j the aperture size.

The scattered field from all resonators is a sum of the waves scattered from each resonator:

$$u_{\rm sc}(\boldsymbol{r}) = \sum_{j=1}^{J}\sum_{n=-\infty}^{\infty} f_n^j \mathrm{U}_n(k\boldsymbol{r} - k\boldsymbol{r}_j), \tag{14}$$

where $\boldsymbol{r}$ cannot be within any resonator, J is the total number of resonators, and f_n^j are the scattering coefficient of the j-th resonator as introduced in section **Scattering by a single resonator**.

For numerical validation, and to help explain the ensemble averaging, it helps to specialise to the case of all resonators within a large sphere. To achieve this we use Graf's addition theorem, to rewrite (14) in terms of outgoing waves centred as the origin:

$$u_{\rm sc}(\boldsymbol{r}) = \sum_{j=1}^{J}\sum_{n,n'=-\infty}^{\infty} \mathrm{V}_{n-n'}(-k\boldsymbol{r}_j) f_n^j(\Lambda)\mathrm{U}_{n'}(k\boldsymbol{r}). \tag{15}$$

The coefficients f_n^j depend on all properties and positions of all resonators[20,48]. To make this explicit, and simplify notation, we denote one configuration by Λ, which represents all positions and properties of the resonators. We also define the material scattering coefficients of the whole sphere containing all resonators as:

$$\mathcal{F}_n(\Lambda) = \sum_{j=1}^{J} \sum_{n'=-\infty}^{\infty} \mathrm{V}_{n'-n}(-k\boldsymbol{r}_j) f_{n'}^j(\Lambda),$$

which simplifies (15) into:

$$u_{\mathrm{sc}}(\boldsymbol{r}) = \sum_{n'=-\infty}^{\infty} \mathcal{F}_n(\Lambda)\mathrm{U}_n(k\boldsymbol{r}). \tag{16}$$

To calculate the average response of the metamaterial, we ensemble average over all possible positions, orientations and properties[20,21,39], while assuming that resonators do not overlap, and that any possible configuration Λ_i has the same probability (micro-canonical ensemble), which results in:

$$\langle u_{\mathrm{sc}}(\boldsymbol{r})\rangle = \frac{1}{M}\sum_{i=1}^{M}\sum_{n=-\infty}^{\infty} \mathcal{F}_n(\Lambda_i)\mathrm{U}_n(k\boldsymbol{r}) = \sum_{n=-\infty}^{\infty} \langle \mathcal{F}_n\rangle \mathrm{U}_n(k\boldsymbol{r}), \tag{17}$$

where the bracket notation $\langle \circ \rangle$ denotes the ensemble average of $\circ$, and M is the number of possible configurations Λ_i which tends to infinite.

The average material coefficients $\langle \mathcal{F}_n \rangle$ can be calculated either by the effective waves method[20,44], or by brute force Monte-Carlo simulations using the Julia library MultipleScattering.jl[49].

The effective waves method calculates the average amplitude (17) directly, avoiding the explicit computation of the scattering from each configuration (16). Further, this method provides a semi-analytic formula for the dispersion equation of the meta-material, which we use to obtain a low-frequency expansion in section **Low-frequency expansion**, resulting in explicit formulae for the effective-properties.

On the other hand, Monte-Carlo simulations estimate the average response by explicitly calculating the scattering from each configuration Λ_i, repeating this for a very large number of possible configurations, and then calculating the average (17). This strategy also allows the computation of higher statistical moments of the scattered field, such as the mean scattered intensity:

$$\langle |u_{\mathrm{sc}}(\boldsymbol{r})|^2\rangle = \sum_{n,m=-\infty}^{\infty} \langle \mathcal{F}_n^* \mathcal{F}_m\rangle \mathrm{U}_n^*(k\boldsymbol{r})\mathrm{U}_m(k\boldsymbol{r}), \tag{18}$$

where * means complex conjugation. In section **Monte-Carlo validation**, we used both the mean amplitude (17) and mean intensity (18) calculated from Monte-Carlo simulations for our disordered metamaterial, and compare them against the average response from the effective-properties (1) deduced in section **Low-frequency expansion**.

It is interesting to compare the average intensity against the intensity of the average to illustrate attenuation due to phase cancellation. The Cauchy-Schwarz inequality applied to (17) and (18) leads to:

$$\langle |u_{\mathrm{sc}}(\boldsymbol{r})|^2\rangle \geq |\langle u_{\mathrm{sc}}(\boldsymbol{r})\rangle|^2. \tag{19}$$

In other words the "energy" of the average field $|\langle u_{\mathrm{sc}}(\boldsymbol{r})\rangle|^2$ is less than, or equal to, the average energy $\langle |u_{\mathrm{sc}}(\boldsymbol{r})|^2\rangle$. This apparent energy loss in the average field is due to phase cancellation. This effect is illustrated in Fig. 7, where the mean intensity is consistently higher than the mean amplitude for moderate to high frequencies ($ka > 0.2$).

Low-frequency expansion

In this section, we use the dispersion equation for a 2D random particulate material from the effective waves method in [equation 4.10 [44]] to derive effective-properties of the metamaterial with resonators. The single species (one type of particle) version of this dispersion relation is the same as found in[21,50]. As we are interested in the long wavelength regime, we assume that the resonators' positions, orientations, and properties are uncorrelated, except that the resonators cannot overlap. To reach a dispersion equation we also need a closure assumption. We use the Quasi-Crystalline Approximation discussed in[21,51]. For these assumptions, the dispersion equation [equation 4.10 [44]] simplifies to:

$$F_m(\lambda_1) + \sum_{n'=-\infty}^{\infty} \frac{2\pi \overline{T}_n(\lambda_1)}{k_\star^2 - k^2} \int \mathrm{N}_{n'-m}[k(b_1+b_2), k_\star(b_1+b_2)] F_{n'}(\lambda_2)\mathfrak{n}(\lambda_2)\mathrm{d}\lambda_2 = 0, \tag{20}$$

where $\mathrm{N}_n[x,y] = x\mathrm{H}_n'(x)\mathrm{J}_n(y) - y\mathrm{J}_n'(y)\mathrm{H}_n(x)$, $\mathfrak{n}(\lambda)$ is the number density of resonators of type λ, $k_\star$ is the effective wavenumber, $\overline{T}_n(\lambda)$ is the isotropic T-matrix (13) derived in section **T-matrix of a single resonator**, and F_n is the amplitude of the effective wave, defined in[44].

We define the effective speed of sound as follows:

$$c_* = ck/k_\star.$$

To do an asymptotic expansion, we assume there is a maximum outer radius for the resonators $b_{\max}$, such that $b_j \leq b_{\max}$ for all j. We also recall that all resonators are sub-wavelength, so the dimensionless wavenumber $\epsilon = kb_{\max}$ is small. Then, we expand both the speed of sound and effective wavenumber as a power series of ϵ:

$$\frac{c}{c_*} = \chi + \mathcal{O}(\epsilon) \text{ and } k_\star b_j = \chi\alpha_j\epsilon + \mathcal{O}(\epsilon^2), \tag{21}$$

where $\alpha_j = b_j/b_{\max}$, and χ has yet to be determined.

To determine χ we need to perform an asymptotic expansion of the terms in (20), including $\overline{T}_n(\lambda_1)$ which depends on the resonance factor. The trick to do this elegantly is to make no assumptions about the asymptotic order of $z(\lambda)$ [25,26]. This is because $z(\lambda)$ depends on the frequency in a non-trivial way, involving all parameters of the resonators internal geometry (see (6) in section **Scattering by a single resonator**; and (27) and (28) in section **Low-frequency behaviour of the resonance factor**). Fortunately, we can reach simple formulae without making any assumption about $z(\lambda)$. Instead, the resulting error of our method will be relative to $z(\lambda)$.

Performing an asymptotic expansion on the terms in (20) results in:

$$\begin{aligned}
&\tfrac{1}{k_\star^2 - k^2} = \tfrac{b_{\max}^2}{\chi^2 - 1}\tfrac{1}{\epsilon^2} + \mathcal{O}(\epsilon^{-1}),\\
&\mathrm{N}_{n'-m}(kb_{1,2}, k_\star b_{1,2}) = \mathrm{N}^{(0)}_{n'-m}(\chi) + \mathcal{O}(\epsilon), \quad \text{with} \quad \mathrm{N}^{(0)}_n(\chi) = \tfrac{2\mathrm{i}}{\pi}\sum_{m=-\infty}^{\infty}\chi^{|m|}\delta_{n,m},\\
&\overline{T}_n(\lambda_1) = \overline{T}_n^{(2)}(\lambda_1)\alpha_1^2\epsilon^2 + \mathcal{O}(\epsilon^3(1+z(\lambda))), \quad \text{with}\\
&\overline{T}_n^{(2)}(\lambda_1) = \tfrac{\mathrm{i}\pi}{4}\left[\delta_{n,1} + \delta_{n,-1} - \delta_{n,0} + z(\lambda_1)\delta_{n,0}\right].
\end{aligned} \tag{22}$$

where $\delta_{n,m}$ is the delta Kronecker symbol. We have included $z(\lambda)$ in the error so that we do not need to make assumptions about the size of $z(\lambda)$ which can be large. Fortunately, this works well, as the maximum relative error of the leading order term for $\overline{T}_n$ is ϵ. We see this trend in the numerical validation.

Substituting (22) into (20), and retaining only the leading order terms we reach:

$$F_n(\lambda_1) - \frac{2\pi b_{\max}^2}{1-\chi^2}\overline{T}_n^{(2)}(\lambda_1)\alpha_1^2 \sum_{n'=-1}^{1} \mathrm{N}^{(0)}_{n'-n}(\chi) \int F_{n'}(\lambda_2)\mathfrak{n}(\lambda_2)\mathrm{d}\lambda_2 = 0, \tag{23}$$

where the sum is truncated to three terms as the other terms are of higher order in ϵ. To determine χ we multiply both sides of (23) by $\mathfrak{n}(\lambda_1)$ and

integrate over λ_1, leading to the following eigenvalue problem:

$$\sum_{n'=-1}^{1} \mathrm{M}_{nn'}\widetilde{F}_{n'} = 0, \text{ with } \widetilde{F}_n = \int F_n(\lambda_1)\mathfrak{n}(\lambda_1)\mathrm{d}\lambda_1 \text{ and } \mathrm{M}_{nn'} = \delta_{n,n'} - \frac{2\pi b_{\max}^2}{1-\chi^2}\mathrm{N}^{(0)}_{n'-n}(\chi)\int \overline{T}^{(2)}_n(\lambda_1)\alpha_1^2\mathfrak{n}(\lambda_1)\mathrm{d}\lambda_1. \tag{24}$$

By solving the dispersion relation $\det \mathrm{M} = 0$, we can obtain an exact expression for χ which substituted into (21) leads to (at leading order):

$$c_*^2 = \frac{\beta}{\rho}\frac{(1-\varphi)}{(1-\varphi+\sum_{j=1}^{N} z(\lambda_j)\phi_j)(1+\varphi)}, \tag{25}$$

where, to simplify the exposition, we have specialised the above to a mixture of N types of resonators which led us to substitute

$$\mathfrak{n}(\lambda) = \sum_{j=1}^{N}\frac{\phi_j}{\pi b_j^2}\delta(\lambda-\lambda_j), \tag{26}$$

where ϕ_j is the volume fraction of the resonator of type j, $\varphi = \sum_{j=1}^{N}\phi_j$ is the total volume fraction of resonators, and δ is the Dirac delta distribution.

Finally, we want an effective density $\rho_\star$ and bulk modulus $\beta_\star$ such that $c_\star^2 = \beta_\star/\rho_\star$. Analogous to[19,20] there is only one way to factor out $\beta_\star$ and $\rho_\star$ such that the limits $\phi_j \to 0$ are consistent, and they lead to (1) presented in section **Results**. Then, to calculate the average response of any metamaterial, one can replace it with an effective homogeneous medium with properties given by (1). We validate these results against Monte-Carlo simulations in Figs. 7 to 9.

We note that it is expected that Helmholtz resonators, with only one gap such as the examples shown in Fig. 10, only significantly alter the effective bulk modulus, as we deduced in (1). This is because one gap leads to a dominant monopole term, and the monopole terms from the resonators contribute to the effective bulk modulus while the dipole terms contribute to the effective density. Therefore a dipole dominant resonator would lead to a significant change in the effective density.

Low-frequency behaviour of the resonance factor

In this section we show $z(\lambda)$ for a 2D thin walled-split resonator. Other expressions for $z(\lambda)$ for other Helmholtz resonators can be deduced from[24,52,53]

We use the results from[22], where $z(\lambda)$ is related to the function $h(\lambda)$ through:

$$z(\lambda) = \frac{2\mathrm{i}}{\pi(kb)^2 h(\lambda)}. \tag{27}$$

For a thin-walled Helmholtz resonator ($b = a$ in Fig. 1) $h(\lambda)$ is given by [equation (3.7) [22]]:

$$h(kb, k\ell) = 2 + \frac{4\mathrm{i}}{\pi}(\gamma_e + \log\frac{k\ell}{4}) - \frac{1}{2}\sum_{m=-\infty}^{\infty}\frac{\mathrm{Q}_{\mathrm{m}^2(\mathrm{kb})}}{\mathrm{H}'(kb)\mathrm{J}'(kb)}, \tag{28}$$

where $\mathrm{Q}_m(x) = \mathrm{J}_m(x)\mathrm{H}'_m(x) + \mathrm{J}'_m(x)\mathrm{H}_m(x)$ and γ_e is the Euler-Mascheroni constant. For the expression for $h(kb, ka, k\ell)$ for a thick-walled resonator ($a < b$) see [equation (3.7) [22]], which we use to produce the results in Fig. 6.

Performing the asymptotic expansion of $\epsilon = kb \ll 1$ in (28) we obtain

$$h(kb, k\ell) = 2 + \frac{4\mathrm{i}}{\pi}(\gamma_e + \log\frac{k\ell}{4}) + \frac{2\mathrm{i}}{\pi}\frac{1}{\epsilon^2} + \mathcal{O}\left(\frac{1}{\epsilon}\right), \tag{29}$$

where we do not expand the logarithmic term. From the above, and noting that $k\ell < kb$, we can conclude that $|h| \in \mathcal{O}(\epsilon^{-2})$ for frequencies away from resonance, which implies that $|z| \in \mathcal{O}(1)$. At resonance we have that $h(\lambda)$ is purely real, which occurs when $h(kb, k\ell) = 2$, and then $|z| \in \mathcal{O}(\epsilon^{-2})$. In other words, $z(\lambda)$ changes its order in ϵ when passing through resonance, which complicates an asymptotic analysis. Luckily, we do not need to perform an asymptotic expansion on $z(\lambda)$ to deduce simple effective formulae for the leading order term.

Data availability

The data that support the findings of this study are openly available at the following https://doi.org/10.5281/zenodo.17226628.

Code availability

The code that supports the findings of this study is openly available at the following https://doi.org/10.5281/zenodo.17226628.

Received: 7 May 2025; Accepted: 27 January 2026;
Published online: 03 March 2026

References

1. Failla, G., Marzani, A., Palermo, A., Russillo, A. F. & Colquitt, D. Current developments in elastic and acoustic metamaterials science. *Philos. Trans. R. Soc. A: Math. Phys. Eng. Sci.* **382**, 20230369 (2024).
2. Shelby, R. A., Smith, D. R. & Schultz, S. Experimental verification of a negative index of refraction. *Science* **292**, 77–79 (2001).
3. Banerjee, B. *An introduction to metamaterials and waves in composites* (Taylor & Francis, 2011).
4. Cummer, S. A. & Schurig, D. One path to acoustic cloaking. *N. J. Phys.* **9**, 45 (2007).
5. Parnell, W. J. & Shearer, T. Antiplane elastic wave cloaking using metamaterials, homogenization and hyperelasticity. *Wave Motion* **50**, 1140–1152 (2013).
6. Pendry, J. B., Schurig, D. & Smith, D. R. Controlling electromagnetic fields. *Science* **312**, 1780–1782 (2006).
7. Norris, A. & Shuvalov, A. Elastic cloaking theory. *Wave Motion* **48**, 525–538 (2011).
8. Nassar, H. et al. Nonreciprocal acoustic and elastic materials. *Nat. Rev. Mater.* **5**, 667–685 (2020).
9. Lawrence, A. J., Goldsberry, B. M., Wallen, S. P. & Haberman, M. R. Numerical study of acoustic focusing using a bianisotropic acoustic lens. *J. Acoustical Soc. Am.* **148**, EL365–EL369 (2020).
10. Yang, M., Chen, S., Fu, C. & Sheng, P. Optimal sound-absorbing structures. *Mater. Horiz.* **4**, 673–680 (2017).
11. Groby, J.-P. et al. Enhancing the absorption properties of acoustic porous plates by periodically embedding helmholtz resonators. *J. Acoustical Soc. Am.* **137**, 273–280 (2015).
12. Boulvert, J., Gabard, G., Romero-Garcia, V. & Groby, J.-P. Compact resonant systems for perfect and broadband sound absorption in wide waveguides in transmission problems. *Sci. Rep.* **12**, 10013 (2022).
13. Jiménez, N., Huang, W., Romero-García, V., Pagneux, V. & Groby, J.-P. Ultra-thin metamaterial for perfect and quasi-omnidirectional sound absorption. *Appl. Phys. Lett.* **109**, 121902 (2016).
14. Meng, Y. et al. Minimum-phase reflection for a passive acoustic absorber with target absorption spectrum and minimum volume. *Phys. Rev. Appl.* **22**, 064074 (2024).
15. Kumar, S., Tan, S., Zheng, L. & Kochmann, D. M. Inverse-designed spinodoid metamaterials. *Npj Comput. Mater.* **6**, 1–10 (2020).
16. Mao, S. et al. Multi-task topology optimization of photonic devices in low-dimensional fourier domain via deep learning. *Nanophotonics* **12**, 1007–1018 (2023).
17. Askari, M. A. et al. Additive manufacturing of metamaterials: A review. *Addit. Manuf.* **36**, 101562 (2020).
18. Fan, J. et al. A review of additive manufacturing of metamaterials and developing trends. *Mater. Today* **50**, 303–328 (2021).
19. Martin, P. A., Maurel, A. & Parnell, W. J. Estimating the dynamic effective mass density of random composites. *J. Acoustical Soc. Am.* **128**, 571–577 (2010).

20. Gower, A. L. & Kristensson, G. Effective waves for random three-dimensional particulate materials. *N. J. Phys.* **23**, 063083 (2021).
21. Gower, A. L., Smith, M. J. A., Parnell, W. J. & Abrahams, I. D. Reflection from a multi-species material and its transmitted effective wavenumber. *Proc. R. Soc. A: Math., Phys. Eng. Sci.* **474**, 20170864 (2018).
22. Smith, M. J. A., Cotterill, P. A., Nigro, D., Parnell, W. J. & Abrahams, I. D. Asymptotics of the meta-atom: plane wave scattering by a single Helmholtz resonator. *Phil. Trans. R. Soc. A* **380**, 20210383 (2022).
23. Sheng, P. & van Tiggelen, B.*Introduction to wave scattering, localization and mesoscopic phenomena*. (Taylor & Francis, 2007).
24. Krynkin, A., Umnova, O., Chong, A. Y. B., Taherzadeh, S. & Attenborough, K. Scattering by coupled resonating elements in air. *J. Phys. D: Appl. Phys.* **44**, 125501 (2011).
25. Smith, M. J. A. & Abrahams, I. D. Tailored acoustic metamaterials. Part I. Thin- and thick-walled Helmholtz resonator arrays. *Proc. R. Soc. A* **478**, 20220124 (2022).
26. Smith, M. J. A. & Abrahams, I. D. Tailored acoustic metamaterials. Part II. Extremely thick-walled Helmholtz resonator arrays. *Proc. R. Soc. A* **478**, 20220125 (2022).
27. Bakhvalov, N. & Panasenko, G.*Homogenisation: Averaging Processes in Periodic Media: Mathematical Problems in the Mechanics of Composite Materials* (Kluwer Academic Publishers, Dordrecht, 1989).
28. Parnell, W. & Abrahams, I. Homogenization for wave propagation in periodic fibre-reinforced media with complex microstructure. i-"theory. *J. Mech. Phys. Solids* **56**, 2521–2540 (2008).
29. Vanoni, C., Kim, J., Steinhardt, P. J. & Torquato, S. Dynamical properties of particulate composites derived from ultradense stealthy hyperuniform sphere packings. *Phys. Rev. E* **112**, 015406 (2025).
30. Sellami, A., Franklin, H., Njeh, A. & Maréchal, P. Effective bulk and mass densities of randomly distributed coated cylinders in fluid. *J. Acoustical Soc. Am.* **157**, 409–419 (2025).
31. Torrent, D., Håkansson, A., Cervera, F. & Sánchez-Dehesa, J. Homogenization of two-dimensional clusters of rigid rods in air. *Phys. Rev. Lett.* **96**, 204302 (2006).
32. Torrent, D. & Sánchez-Dehesa, J. Effective parameters of clusters of cylinders embedded in a nonviscous fluid or gas. *Phys. Rev. B.* **74**, 224305 (2006).
33. Torrent, D. & Sánchez-Dehesa, J. Acoustic metamaterials for new two-dimensional sonic devices. *N. J. Phys.* **9**, 323 (2007).
34. Torrent, D. & Sánchez-Dehesa, J. Multiple scattering formulation of two-dimensional acoustic and electromagnetic metamaterials. *N. J. Phys.* **13**, 093018 (2011).
35. Guérin, C.-A., Mallet, P. & Sentenac, A. Effective-medium theory for finite-size aggregates. *J. Opt. Soc. Am. A* **23**, 349–358 (2006).
36. Markel, V. A. & Tsukerman, I. Current-driven homogenization and effective medium parameters for finite samples. *Phys. Rev. B* **88**, 125131 (2013).
37. Sun, R., Lem, J., Kai, Y., DeLima, W. & Portela, C. M. Tailored ultrasound propagation in microscale metamaterials via inertia design. *Sci. Adv.* **10**, eadq6425 (2024).
38. Piggott, A. Y. et al. Inverse design and demonstration of a compact and broadband on-chip wavelength demultiplexer. *Nat. Photonics* **9**, 374–377 (2015).
39. Foldy, L. L. The multiple scattering of waves. i. general theory of isotropic scattering by randomly distributed scatterers. *Phys. Rev.* **67**, 107–119 (1945).
40. Karnezis, A. & Gower, A. L. Calculating pair-correlations from random particle configurations. *preprint arXiv:2401.09236* (2024).
41. Pinfield, V. J. & Valier-Brasier, T. Multimode multiple wave scattering in suspensions of solid particles in viscous liquids: part 2: numerical validation. *Proc. R. Soc. A* **480**, 20240106 (2024).
42. Rohfritsch, A., Conoir, J.-M., Marchiano, R. & Valier-Brasier, T. Numerical simulation of two-dimensional multiple scattering of sound by a large number of circular cylinders. *J. Acoustical Soc. Am.* **145**, 3320–3329 (2019).
43. Gower, A. L., Hawkins, S. C. & Kristensson, G. A model to validate effective waves in random particulate media: spherical symmetry. *Proc. R. Soc. A* **479**, 20230444 (2023).
44. Napal, K. K., Piva, P. S. & Gower, A. L. Effective t-matrix of a cylinder filled with a random two-dimensional particulate. *Proc. R. Soc. A: Math., Phys. Eng. Sci.* **480**, 20230660 (2024).
45. Karnezis, A., Piva, P. S. & Gower, A. L. The average transmitted wave in random particulate materials. *N. J. Phys.* **26**, 063002 (2024).
46. Waterman, P. Matrix formulation of electromagnetic scattering. *Proc. IEEE* **53**, 805–812 (1965).
47. Waterman, P. C. Symmetry, unitarity, and geometry in electromagnetic scattering. *Phys. Rev. D.* **3**, 825–839 (1971).
48. Martin, P. A.*Multiple Scattering: Interaction of Time-Harmonic Waves with N Obstacles* (Cambridge University Press, Cambridge, UK, 2006).
49. Gower, A. L. & Deakin, J. Multiplescatering.jl: A julia library for simulating, processing, and plotting multiple scattering of waves. version 0.1.21. https://github.com/JuliaWaveScattering/MultipleScattering.jl Github (2024).
50. Linton, C. & Martin, P. Multiple scattering by random configurations of circular cylinders: Second-order corrections for the effective wavenumber. *J. Acoustical Soc. Am.* **117**, 3413–3423 (2005).
51. Piva, P. S., Napal, K. K. & Gower, A. L. Acoustic waves in a halfspace material filled with random particulate. *N. J. Phys.* **26**, 123033 (2024).
52. Skvortsov, A. T., MacGillivray, I. R. & Godin, O. A. Acoustic waves in a perforated cylinder. *J. Acoustical Soc. Am.* **157**, 1880–1888 (2025).
53. Rao, T. C. & Barakat, R. Plane wave scattering from a cylindrical helmholtz resonator: Dirichlet case. *Opt. Commun.* **164**, 223–232 (1999).

Acknowledgements

The authors would like to thank the Isaac Newton Institute for Mathematical Sciences, Cambridge, for support and hospitality during the programme Mathematical Theory and Applications of Multiple Wave Scattering, where work on this paper was undertaken. This work was supported by EPSRC grant EP/R014604/1. Paulo Piva gratefully acknowledges funding from an EPSRC Case studentship with Johnson Matthey. Art Gower gratefully acknowledges support from EPSRC (EP/V012436/1). David Abrahams gratefully acknowledges funding from the Royal Society for an Industry Fellowship with Thales UK.

Author contributions

P.S.P.: conceptualization, formal analysis, investigation, coding, figures, validation, writing first draft, review and editing; A.L.G.: conceptualization, formal analysis, investigation, coding, review and editing; I.D.A.: conceptualization, formal analysis, investigation, review and editing.

Competing interests

The authors declare no competing interests.

Additional information

Correspondence and requests for materials should be addressed to Art L. Gower.

Reprints and permissions information is available at http://www.nature.com/reprints

Publisher's note Springer Nature remains neutral with regard to jurisdictional claims in published maps and institutional affiliations.

Open Access This article is licensed under a Creative Commons Attribution-NonCommercial-NoDerivatives 4.0 International License, which permits any non-commercial use, sharing, distribution and reproduction in any medium or format, as long as you give appropriate credit to the original author(s) and the source, provide a link to the Creative Commons licence, and indicate if you modified the licensed material. You do not have permission under this licence to share adapted material derived from this article or parts of it. The images or other third party material in this article are included in the article's Creative Commons licence, unless indicated otherwise in a credit line to the material. If material is not included in the article's Creative Commons licence and your intended use is not permitted by statutory regulation or exceeds the permitted use, you will need to obtain permission directly from the copyright holder. To view a copy of this licence, visit http://creativecommons.org/licenses/by-nc-nd/4.0/.

© The Author(s) 2026